Role of Multiple-Contact Miscibility in Drainage from a Two-Dimensional Porous Medium

Hanbang Zou,[1] Anja C. Slim,[2,3,*] and Adrian Neild[1,†]

[1] *Department of Mechanical and Aerospace Engineering, Monash University, Clayton, Victoria 3800, Australia*
[2] *School of Mathematics, Monash University, Clayton, Victoria 3800, Australia*
[3] *School of Earth, Atmosphere and Environment, Monash University, Clayton, Victoria 3800, Australia*

(Received 22 December 2020; revised 9 March 2021; accepted 22 April 2021; published 18 May 2021)

We carry out a comprehensive series of experiments to understand the effect of multiple-contact miscibility on drainage from a porous medium. Our experiments are performed using a microfluidic porous medium consisting of a random distribution of cylindrical pillars to create a two-dimensional heterogeneous network of pores. A mixture of ethanol and 1-hexanol is injected into the porous medium as a wetting reservoir phase. A mixture of water and ethanol is subsequently injected to displace the reservoir phase. Depending on the precise composition of these two phases, they can be immiscible, develop miscibility over time through mass transfer between them, or be immediately miscible. We describe the distinct behaviors observed depending on the composition and injection flow rate and compare and contrast them with the classical parameter regime diagram for drainage displacement of R. Lenormand *et al*. [J. Fluid Mech. 189, 165 (1988)]. When the system is immiscible, the injection rate is the dominant control and the behavior is broadly classical. In systems that develop miscibility for the compositions we explore, the fluids remain immiscible at the injection tip and develop miscibility further upstream. Trapped regions of reservoir fluid are mobilized over time through the development of miscibility. For systems that nearly develop miscibility, trapped regions are mobilized at sufficiently high flow rates. We also show that the porosity has limited impact on the behavior and phase-saturation level. Our work has applications to carbon-dioxide enhanced oil recovery.

DOI: 10.1103/PhysRevApplied.15.054040

I. INTRODUCTION

Microfluidic channels can be constructed so that they have features patterned with a spacing that has a similar length scale to the pores of rocks. These rock-on-a-chip systems can be formed by using a channel filled with a packed bed of beads, with the bead diameter dictating the dimensions of the porous network formed within the bed. Alternatively, the use of regularly or randomly spaced pillars can be used; in this way the system is reduced to two dimensions, which aids visual accessibility and allows pore-scale interrogation of fluid behavior [1]. Typically, such a microfluidic rock is initially flooded with one phase, and subsequently a second injection phase is used to displace this reservoir phase.

Numerous studies have investigated the displacement of the reservoir phase by an immiscible injection fluid, and characterized this across a range of capillary numbers and viscosity ratios [2–8]. At low flow rates, when a nonwetting phase displaces a wetting phase, the process is governed by capillary forces. The injected fluid invades a pore when the pressure across the interface between the two fluids is in excess of the capillary threshold, which is given by $P = 2\sigma\cos(\theta)/R$, where σ is the interfacial tension between the injected phase and the reservoir phase, θ is the contact angle measured through the wetting fluid, and R is an effective radius characterizing the size of the pore throat and its geometry. Hence there is preferential invasion of larger pores having lower capillary pressures. The invasion process is broadly understood, although the details are complex and have been the subject of significant recent research [9,10]. At higher flow rates, viscous effects are increased, the pore-entry pressures no longer dictate invasion and the invading fluid can advance through smaller pore throats. In this case, the displacement is normally characterized by two dimensionless parameters, the capillary number Ca and the viscosity ratio between the invading and reservoir fluids. Lenormand *et al.* [6] carried out a series of drainage experiments in a microfluidic porous medium across this parameter space and delineated three regimes of flow behavior, namely capillary fingering, viscous fingering, and stable displacement. The term fingering is used to describe a highly uneven

*anja.slim@monash.edu
†adrian.neild@monash.edu

fluid front, with significant differences in the progression of the injection fluid across the width of the system. Capillary fingering occurs when the capillary number is very low so that the viscous forces in both fluids are negligible, and corresponds to the invasion behavior described above. Viscous fingering is observed when a low-viscosity fluid displaces a more viscous fluid at a high flow rate, leading to a relatively low pressure drop along the injected stream. The stable displacement regime occurs when a low-viscosity fluid is displaced by a relatively viscous fluid at a high injection rate, and results in high injected-phase saturation.

An extension to the studies described above is the effect of an evolving miscibility between the two fluids. If the two phases consist of three components from a ternary system, then depending on their relative concentrations, the two phases can be immiscible, multiple-contact miscible (MCM), or first-contact miscible (FCM). FCM is a status when two phases mix instantly, whereas MCM is when two phases gradually become miscible due to the exchange of chemical components between them. There are significantly fewer rock-on-a-chip characterization studies of MCM systems than immiscible ones, despite an example of such a system being carbon-dioxide enhanced oil recovery (CO_2 EOR). Once oil production declines from an established field, enhanced recovery methods can be used to extend its life. In CO_2 EOR, pressurized CO_2 is injected into the well. Here, the three components, themselves a simplification of the multicomponent oil-gas systems, are CO_2 and lean components, light intermediates, and heavier intermediates [11–14]. Under the right conditions, multiple-contact miscibility can develop, enabling the extraction of further oil from the reservoir. To identify whether the requisite conditions are met at a given reservoir, both macro- and microsystems have been developed to test for the development of miscibility. MCM displacement can be achieved via a condensing process, a vaporizing process or a combined condensing and vaporizing process [15–17]. As the injected phase proceeds through the pore space, the vaporization of lighter components from the fresh reservoir phase into the invading phase front can lead to miscibility. This is known as a vaporizing process. Similarly, the displacement where miscibility is achieved due to transfer of the lighter components from the fresh injected phase into the trapped reservoir phase near the injection site is termed a condensing process [15–19]. Bahralolom *et al.* [20] first visualized macroscale features of preferential displacement paths between CO_2 and crude oil in an etched glass micro model. Al-Wahaibi [21] added variable permeability of the porous medium on first-contact and multiple-contact miscible displacement in a glass-bead micromodel. Their main focus was on the phase evolution, analyzed via effluent composition measurements. However, neither study probed the pore-scale dynamical behavior of the trapped reservoir phase and invading phase at different locations during MCM, and this still requires further exploration.

Key parameters for ternary systems, in the context of fluid displacement, are the conditions under which MCM is possible. Specific to miscible-gas EOR, this may be in terms of the required reservoir pressures [minimum miscible pressure (MMP)] or the composition of the injected fluid [minimum miscible enrichment (MME)]. These conditions can be found using chips in which small volumes of reservoir fluid is trapped in dead-end channels or pockets. The subsequent removal of this fluid can demonstrate the onset of MCM [22,23]. However, these systems neglect the role of wetting and viscous-drag effects within more complex, rocklike channels. In a previous work, we examined the behavior of trapped reservoir fluid within a rock on a chip, and showed how these observations act as a rapid measurement method for identifying miscibility development [24]. We found the removal occurs at concentrations for which the ternary diagram does not predict MCM. This was due to the trapped fluid volumes being mobilized as the interfacial tension between still-immiscible fluids dropped. Hence, when a ternary system is examined in the context of a porous medium, the onset of MCM is not the sole predictor of displacement. To understand the transition between trapped and displaced fluid, in this work, we focus on the pore-scale dynamics and examine the role of composition, flow rate, and pore size. We show a transition region due to shear between injection-dominated regimes to diffusion-dominated regimes. This work is an attempt to extend the classical parameter-space diagram of Lenormand *et al.* [6] for drainage to a partially miscible ternary system.

Our experimental setup and the ternary system we use are described in Sec. II. The analog ternary system consists of water, ethanol, and 1-hexanol. This system is well characterized [25] and has similar phase-evolution trajectories as a simplified ternary oil-gas system [11–14]. Such analog systems have been popular for interrogating partially miscible phase behavior at ambient conditions [21,26–33]. In Sec. III, we first describe experiments with different injected fluid compositions at low flow rates and find dramatic differences in behavior.

Subsequently, we describe the flow dynamics for different porosities and different injection rates. We find that there are only minor differences in the displacement path for the porosity range we consider. In contrast, the injection rate has a significant impact. We summarize our observations in Sec. IV.

II. METHODS

Experiments are carried out using a well-characterized ternary fluid system in a microfluidic porous medium consisting of randomly distributed pillars of various radii. In Sec. II A, the pore network design and fabrication are

described, followed by a description of experiment setup and image analysis in Sec. II B. Two separate simulations are then carried out to guide the interpretation of the data. A comprehensive model that captures both temporal and spatial evolution is complicated and requires a multiple scale model. Our work focuses on experiments and our simulations are indicative. Recently, a study suggests that a model considering both temporal and spatial evolution of a partially miscible system is not far away [34]. In Sec. II C, the theoretical prediction for MME based on a mixing-cell model is described. Subsequently, a numerical preferential path simulation for immiscible flow at low capillary numbers is described in Sec. II D.

The setup of the experiments followed by a description of the theoretical prediction for MME based on a mixing-cell model.

A. Design of the microfluidic porous medium

A schematic of the microfluidic porous medium is shown in Fig. 1(a). The length of the main channel is 20 000 μm, the width is 2500 μm, and the height is 137 μm. The channel is fabricated in poly(dimethylsiloxane) (PDMS) by casting on a patterned substrate, which is created by standard SU8 photolithography. The channel is subsequently peeled from the patterned substrate and plasma bonded to a glass slide coated with a thin uniform layer of PDMS. This construction ensures a symmetrical wetting environment.

The microfluidic channel contains a random distribution of cylindrical pillars of different sizes so as to mimic the variations found in a real reservoir. The algorithm for creating the stochastic network is explained in our previous work [24]. We present data for three different chips, in which the location of the pillars is identical, but the relative size of each pillar is scaled as shown in Fig. 1(b). This approach of using the same randomly generated template for each design allows us to interrogate the impact of varying porosity in isolation of varying heterogeneity of the porous medium. For the smallest pillars (in light brown), the range of radii is from 60 to 100 μm giving a porous medium with 72% porosity. For the intermediate pillars (in brown), the range of radii is from 65 to 105 μm giving 67% porosity. Finally for the largest pillars (in black), the range of radii is 70 to 110 μm yielding 62% porosity.

B. Experimental procedure

A well-characterized ternary system that is chemically compatible with PDMS is used to investigate the development of miscibility in the microfluidic porous medium [25,35]. The system comprised water, ethanol (Merck ethanol ≥99.8%), and 1-hexanol (Sigma-Aldrich 1-hexanol anhydrous ≥ 99%). The temperature is maintained via a Peltier temperature-control system at 35 °C, for which detailed thermodynamic measurements are available [25]. This system can be considered as an analog for CO_2 EOR, with water corresponding to CO_2 and lean hydrocarbon components, ethanol to the light-intermediate hydrocarbons, and hexanol to the heavy-intermediate hydrocarbons [11–13].

In the experiments, the initial composition of the reservoir fluid is fixed at 65% 1-hexanol, 35% ethanol in mole fractions, and the injected fluid composition varied from 100% water, 0% ethanol to 75% water, 25% ethanol. As all the initial phases are prepared as binary solutions with ethanol, the ethanol fraction is omitted in the main text. The injected and reservoir fluid samples are prepared using a pipette (Eppendorf Research), with the desired mole fraction converted into a volume fraction. The largest error

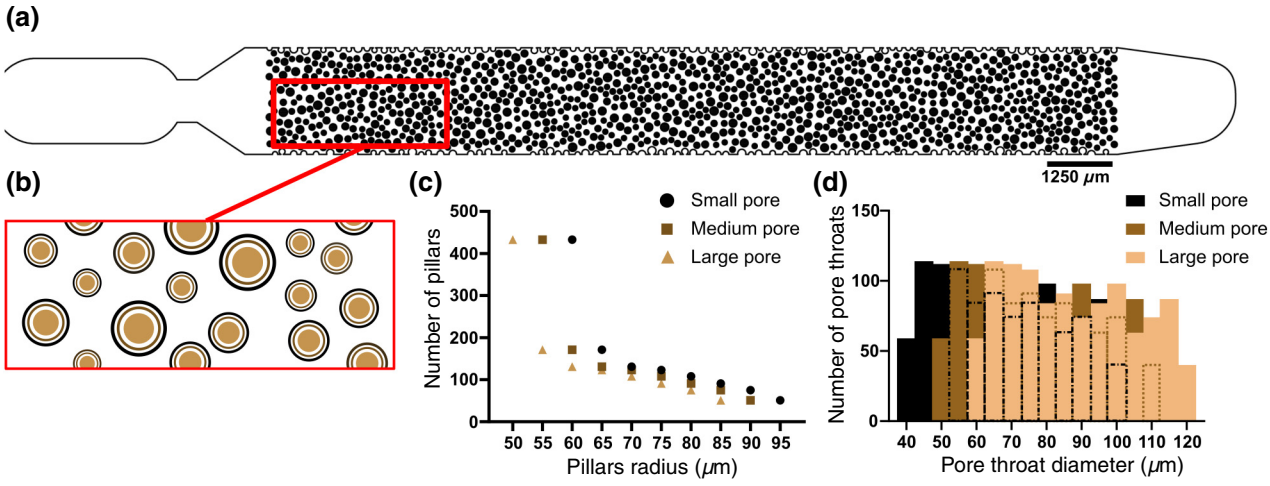

FIG. 1. (a) Schematic of the microfluidic channel illustrating the random distribution of cylindrical pillars. (b) Close up showing the pillars for the three different chips used; the centers of the pillars are the same, but their radii are different. Frequency distributions of (c) pillar radii and (d) pore-throat sizes for the three different chips.

propagation from the pipette is only about ±0.3% at 82% water. Prior to injection into the chip, the samples are mixed by a vortex mixer (ISG 153-010) in a closed micro tube (Kinesis 2.0 ml) with limited ethanol vaporization. Subsequently, the wetting phase (the hexanol-rich phase) is injected into the empty channel to act as the reservoir phase. This phase is subsequently displaced by a second, water-rich, nonwetting injected phase via a flow-rate-controlled pump (KD Scientific Legato 210, Holliston, MA, USA) with a glass syringe (500 μl SETonic glass syringe). The switch between the pumping of the two phases is achieved by use of miniature diaphragm isolation valves (Parker, R9 Valve). The flow rates are 12, 120, and 1200 μl/h, which brought the nominal capillary number $\mathrm{Ca} = \mu V/\sigma$ from 10^{-6} to 10^{-4}. Here, μ is the dynamic viscosity of pure water, V is the Darcy velocity based on single-phase flow through the chip at the given flow rate and σ is the interfacial tension between pure hexanol and pure water [36]. Considering these capillary numbers and a representative viscosity ratio of 0.5 between the injected phase and the reservoir phase (taking the viscosity of pure water as representative of the injected phase [37] and the viscosity of 65% hexanol, 35% ethanol as representative of the reservoir phase [38]), immiscible displacement would be expected to transit from capillary fingering (low saturation level) to stable displacement (high saturation level) [2].

Visualization of the injection process is achieved with fluorescent dye added to the injected water-rich phase (fluorescein, Fluka Analytical). Once the injected phase enters the region of interest, videos are captured using a fluorescent microscope (Olympus BX43) with a digital CCD camera (PixeLink, PL-B7CU). Subsequently, image analysis is conducted in MATLAB. The experiment snapshots of selected time for immiscible cases and MCM cases are converted into binary. Subsequently, the injected fluid saturation and width average saturation measurements are conducted for different concentrations. Width average saturation S_w is the saturation of separate phase fluid every 9.5 μm. The fractal dimension measurements are carried out to quantify the fluorescent displacement patterns using Fraclac in ImageJ software [39]. Fractal dimension D is commonly used to describe the complexity of the preferential path during displacement [10,40]. It is defined as $D_f = \log N / \log(\epsilon)$, where N is the number of self-similar parts and ϵ is the magnification factor. For example, the fractal dimension D of a line or circle is 1 and a square or a disk has fractal dimension $D = 2$. Therefore, the fractal dimension of tow-dimensional preferential paths should be between $1 < D < 2$.

C. Theoretical prediction of phase evolution

The theoretical predictions of the phases' evolution are used to verify the experimental observation, which is based on existing thermodynamic measurements from Lin *et al.* [35]. The details of the theoretical calculations' algorithm from a mixing-cell model are elaborated in an earlier work [22]. Figure 2 summarizes the arguments and shows the ternary diagram for the chemical components. Typically, a ternary diagram features a binodal curve that separates regions in which the concentration of components is such that two phases are formed (inside the curve) from the area covering concentrations, which are miscible. In this case, the binodal curve is created via fitting to existing experimental data from Lin *et al.* [35]. Within the immiscible region, the split of components follows tie lines, three of which are shown, such that the two phases that are formed have the concentrations given by the two points at the intersection of the tie line with the binodal curve. The compositional evolution for a ternary diagram is described by a mixing-cell model, which is a discretized representation of the continuous process [14]. The schematic illustration of this process is shown in Fig. 2. In the example shown, a trapped hexanol-rich reservoir phase of composition T is displaced by a fresh continuous water-rich phase of composition I. Suppose the trapped reservoir fluid is located near the injection site and a small volume of the fresh displacing phase mixes with the trapped reservoir fluid, resulting in a mixture M_1 lying on a dilution line that connects I and T (when the trajectory within the ternary

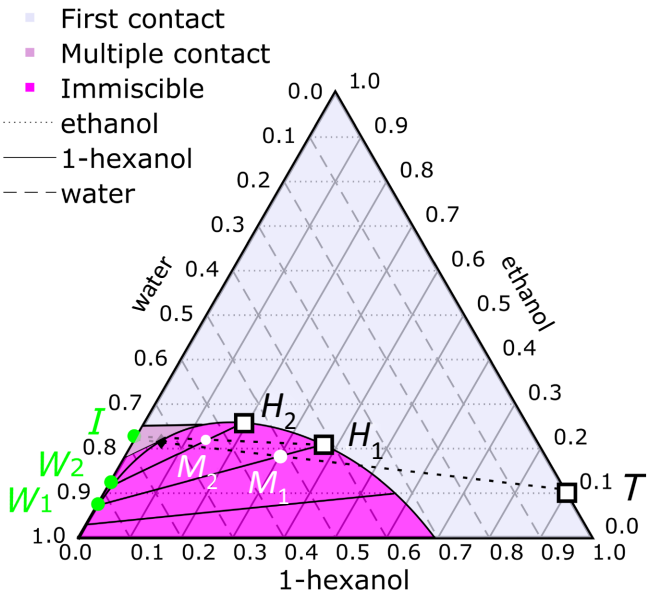

FIG. 2. Ternary phase diagram for the water-ethanol-hexanol ternary system at 35 °C from Lin *et al.* [35]. Compositions are in mole fractions. The curve is the binodal curve. The symbols give a schematic illustration of the compositional evolution in a condensing process between a fresh injected water-rich phase of initial composition I and a static trapped reservoir phase of initial composition T. Schematic evolution is based on a mixing-cell model. Points W_i, M_i, and H_i are explained in the text.

diagram is modeled, the quantity of I added is kept small; here the relative volumes are chosen to make the depiction clear). As it is located within the binodal curve, the mixture separates into two immiscible phases, namely a water-rich phase of composition W_1 and a hexanol-rich phase of composition H_1 located at either end of the tie line passing through M_1. The hexanol-rich phase remains trapped in the pore, while the water-rich phase mixes with the continuous phase and flows downstream. In the next iteration, a fresh volume of the displacing phase is mixed into the evolved pocket (which now has concentration H_1) to form composition M_2. The mixture again splits with a water-rich phase of composition W_2 remaining in the pocket and a hexanol-rich phase of composition H_2 moving downstream. As it repeats, a fresh volume of the displacing phase is mixed into the evolved, trapped reservoir phase to form composition M_2. Again, the mixture separates into two immiscible phases W_2 and H_2. If the dilution line that connects I and the evolved trapped phase H_n does not cross through the binodal curve, the two phases are MCM. In a case that the initial dilution line is already outside the binodal curve, it is considered as FCM. If the dilution line always crosses the binodal curve, then the two phases are not miscible. Thus, the ternary diagram may be divided into three regions depending on whether an injected phase of the given composition is FCM with the trapped phase T (pale purple in Fig. 2), MCM (intermediate shade of purple), or not miscible (magenta).

D. Preferential path simulation

This study covers the transition of displacement behavior as the concentration of the two phases are varied such that they move from being immiscible to multicontact miscible. To provide a starting point, we also compare the experimentally observed invasion path for pure water at low flow rates to simulated paths based on invasion percolation. It indicates the ideal displacement path for immiscible displacement, based just on the fundamental physics, through the heterogeneous porous media. When the injection concentration changes, the deviation from this immiscible path predication helps us to understand how the miscibility affects the preferential path. Our simulation implements a simple form of the invasion percolation model: it includes a mechanism for fluid trapping, but neglects the possibility of retraction of injected fluid from pores that have been invaded. The invasion percolation for two immiscible phase displacements in porous medium was used by Wilkinson and Willemsen [41]. The model is applicable to the displacement of a wetting fluid by an immiscible, nonwetting fluid when capillary forces dominate [41–45]. In our simulations, we read the pillar layout from an image input, and then calculate the pore throat size at each location. Subsequently, an adjacency matrix function is used to connect all the pore throats. We assume

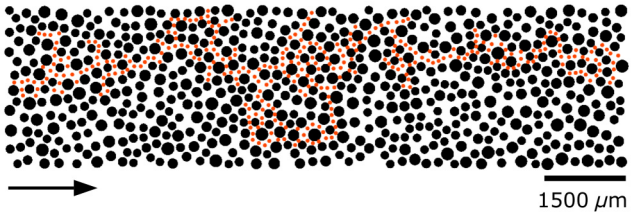

FIG. 3. Results of invasion simulations in the small-pore porous medium used in experiments. Red dots indicate the predicted path.

that the injected nonwetting fluid invades the pore space in sequential steps. At a given step, the neighboring pore with the largest pore throat, and hence the lowest capillary entry pressure, is invaded as shown in Fig. 3. The original theory did not consider the trapping that can occur when the displaced fluid is incompressible [44]. In our simulations, trapping is implemented as follows: when the injected fluid isolates a pocket of the reservoir fluid, such that there is no longer a continuous path of reservoir fluid to the channel exit, that trapped fluid volume can no longer be invaded. The simulation does not take into account any retraction mechanism. Instead, we limit the invasion possibilities to 20 pore throats near the displacement front, which is consistent with previous approaches in which Haines jumps are observed [46,47]. These jumps are a pore-scale effect in which the displacement front of the invading phase penetrates multiple pores in a sequence of sharp interfacial jumps or burst events, which is known to inhibit other pore-space-invading events further upstream [46,48–51].

III. RESULTS AND DISCUSSION

As the literature on pore-scale displacement primarily examines the immiscible case, we begin by describing the dramatic changes observed by varying the concentration of the injected phase, whilst keeping both the pore size and the flow rate constant. We then describe how these behaviors are impacted by flow rates and porosity.

A. Miscibility development

Experimental images at five different instants of time for several different compositions of the injected fluid are shown in Fig. 4(a). The width average saturation (S_w) is measured along the flow direction to characterize the spatial and temporal evolution for immiscible and MCM cases in Figs. 4(b) and 5(b). The sharp drop of the curves indicates the location of invading front at different times. The key of those curves is to use the variation of S_w value at a given location to identify the miscibility condition. In the immiscible cases, there is no variation of S_w curves at a given location between different timestamps. Conversely, in the miscible cases, the S_w value at a given location increases due to miscibility development

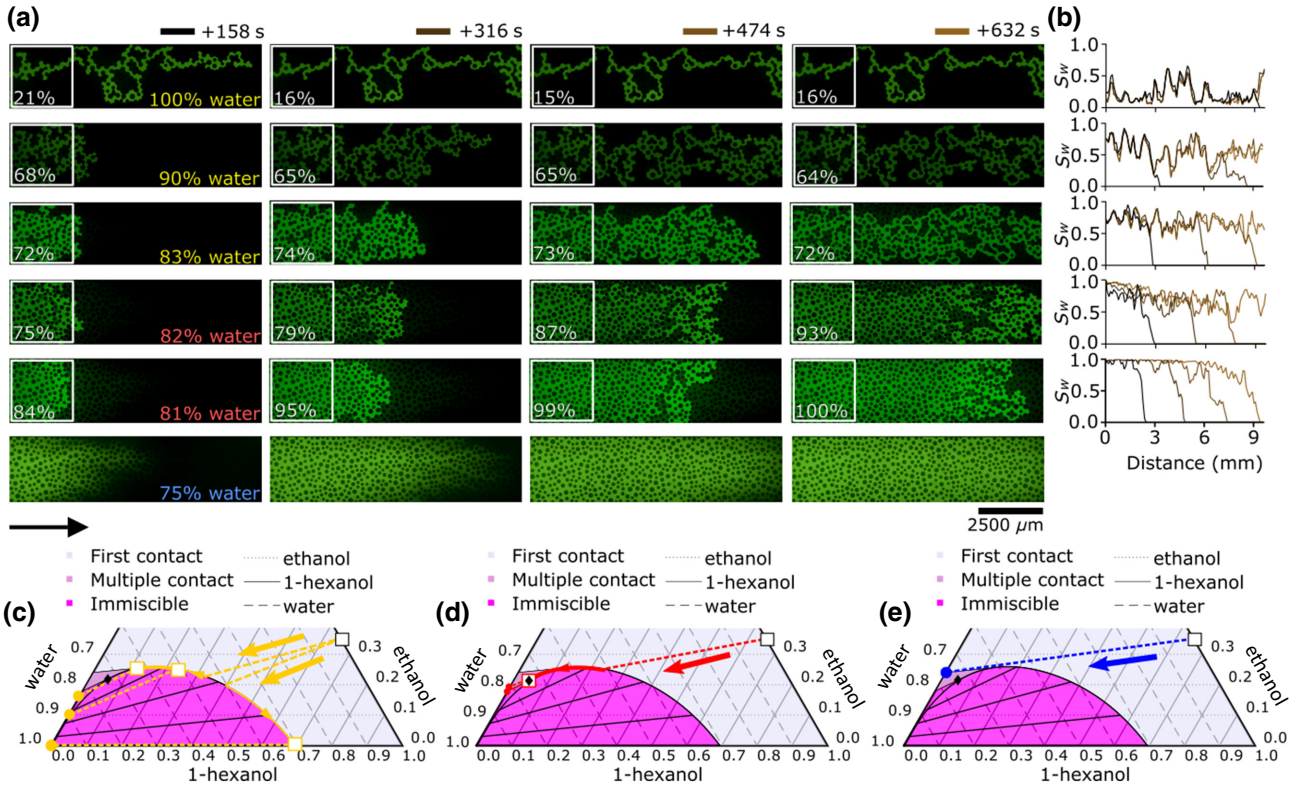

FIG. 4. (a) Experimental snapshots at a selection of times for a wetting reservoir phase (uncolored or black) of initial composition 65% hexanol, 35% ethanol being displaced by injected phases with six different compositions (containing green fluorescein). The injected fluids are mixtures of water and ethanol with the mole fraction of water indicated on each row. Images are of the first half of the microfluidic porous medium. Time zero is the instant at which the advancing front of the injected fluid first contacts a pillar; 790 s is the theoretical time required to fill the pore space in the first half of the channel via complete, stable displacement. The white box is the selected area for injected fluid saturation measurement. (b) Width average saturation (S_w) measured along the flow direction for immiscible (yellow) and MCM cases (red) except the first contact miscible case (blue). Experimental snapshots of selected time (color) are converted into binary images. The injected fluid saturation is subsequently calculated and averaged every 9.5 μm. The values are then normalized with a full saturated image. The figure is added as Fig. S1 within the Supplemental Material using a rearranged and enlarged format so (b) can be seen in greater detail [52]. Panels (c)–(e) show the theoretically predicted compositional pathways of a trapped reservoir fluid (white squares) of initial composition 65% hexanol, 35% ethanol in contact with fresh injected fluid. The injected fluid compositions are indicated by colored dots and correspond to the cases illustrated in (a). In all panels, yellow, red, and blue text and symbols represent immiscible, MCM, and FCM processes. The flow rate is 12 μl/h and the porous medium has the smallest pores (largest pillars) shown in Fig. 1.

as the front moves forward. The corresponding theoretical predictions for the compositional evolution of a trapped reservoir fluid are shown in Figs. 4(c)–4(e). It can be seen that altering the concentration has a significant impact on the configuration of the displacement path as the reduced interfacial tension can no longer trap reservoir fluid in the pore space as effectively.

In the case of an injected phase consisting of pure water, the trapped phase is predicted to lose all its ethanol and eventually consist only of 69% hexanol and 31% water, which is binary immiscible with the fresh injected phase. The figure shows that the injected fluid initially advances along a single convoluted finger, then forms a pocket shape in the middle of the region of interest before subsequently proceeding again as a single finger. Once this structure is established, it is stable over time. The width average saturation measurement in (c) shows unchanged flow structure over time. This behavior is consistent with typical immiscible drainage patterns at capillary numbers around 10^{-6} and a small viscosity contrast between the injected and reservoir phases [2–4,6].

When the water concentration is reduced to 90% or 83%, the fluids are still immiscible [see Fig. 4(c)], but the interfacial tension is reduced and the injected fluid becomes less nonwetting to the host medium. This results in a more stable displacement and increased sweep efficiency, consistent with the behaviors observed for immiscible drainage at higher capillary numbers [3,4,6,9]. The analytical prediction of the composition in Fig. 4(c) shows that the trapped reservoir fluid in these cases absorbs more

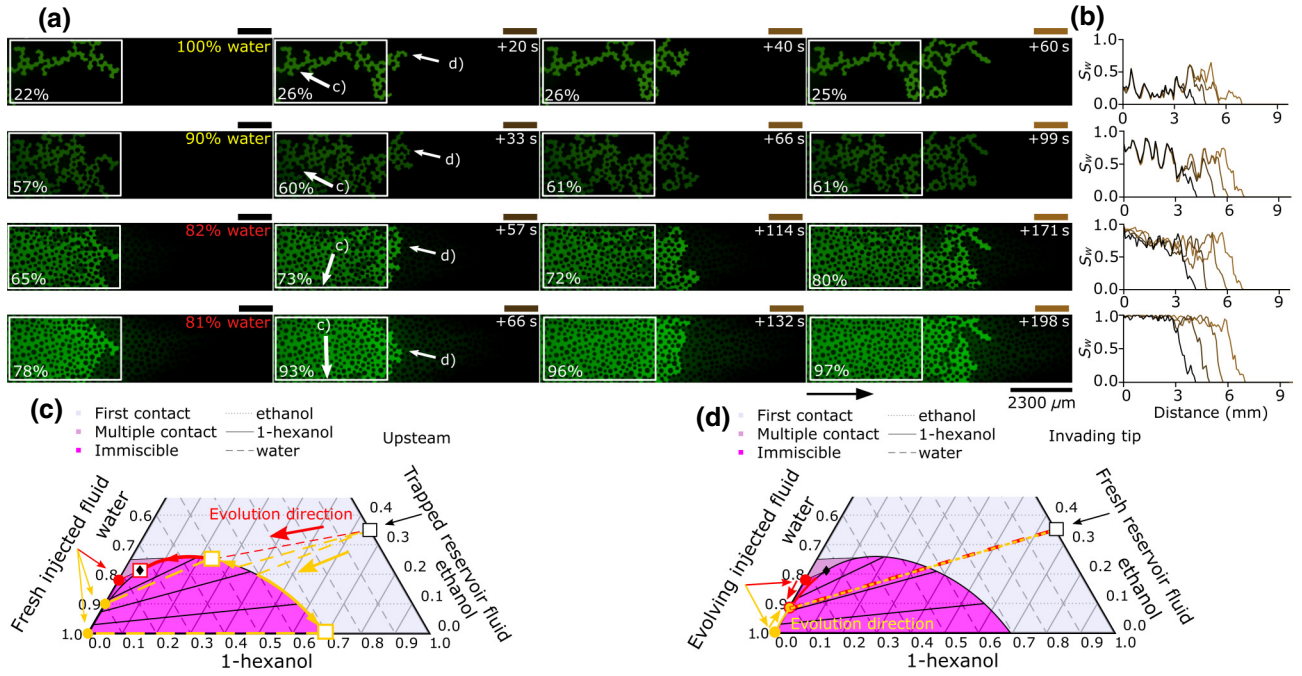

FIG. 5. (a) Experimental snapshots for a wetting reservoir phase (uncolored or black) of initial composition 65% hexanol, 35% ethanol, and four different injected-fluid compositions (containing green fluorescein). The white box is the selected area for injected fluid saturation measurement. (b) Width average saturation (S_w) measured along the flow direction for different time (color). The figure is added as Fig. S2 within the Supplemental Material using a rearranged and enlarged format so (b) can be seen in greater detail [52]. (c) Analytically determined composition routes for a trapped reservoir fluid in a fresh injected phase. The initial reservoir composition is shown by a black-outlined square. The evolution directions are indicated by arrows and the colored squares represent the end locations of the phase evolutions. The composition of the injected fluids are indicated by red and yellow dots. (d) Analytically determined composition routes for a trapped injected fluid in a fresh reservoir phase. The initial injected-fluid compositions are indicated by red and yellow dots and the reservoir phase by a black-outlined square. The flow rate is 12 μl/h and the chip is a large pillar and small pore (62% porosity).

water and loses significantly less ethanol during evolution. As for those cases, once the flow structure of the displacing fluid is established, it remains static because the interfacial tension is still sufficient to overcome the shear forces acting on the trapped reservoir fluid. As shown in Fig. 4(b), the width average saturation remains the same in the channel upstream as the invading tip proceeding forward, indicating the system is immiscible.

When the water concentration is further reduced to 82% or 81%, the trapped reservoir fluid develops miscibility with the injected fluid [see Fig. 4(d)]. The flow structures that develop now continually change over time. As shown in Fig. 4(a), the trapped reservoir fluid at upstream in 82% and 81% cases disappeared as the invading front proceeded forward. This time evolution of the trapped reservoir fluid at upstream is clearly captured in Fig. 4(b). As the invading front proceeds forward, the curves of 82% and 81% cases at the upstream smooth out over time, which indicates the disappearance of the trapped reservoir fluid. Additionally, the overall saturation level of 82% and 81% cases is much higher than the immiscible cases due to lower interfacial tension. In the experiments, the log viscosity ratio ranges from -0.3 to 0.04 with different injected fluid concentrations. The displacement is still in the capillary fingering regime if the two phases are immiscible. However, the miscibility development between two phases significantly reduces the surface tension, which results in a higher capillary number. It means that the displacement moves towards the stable displacement regime, which is consistent with the behaviors observed for immiscible drainage at higher capillary numbers [3,4,6,9]. Therefore, the viscosity ratio plays much less of a role here as surface tension has been altered more with the injected fluid concentration.

Finally, in the 75% water case, the dilution line connecting the injected phase [the blue dot in Fig. 4(e)] and the reservoir phase [the white dot in Fig. 4(e)] is located outside the two-phase region, which means the two fluids are FCM and can mix with each other immediately at any ratio. As shown in the experimental images in Fig. 4(a), the FCM case does not have interfaces between the two phases.

Examining the displacement process in greater detail, we note that there are different multiple-contact processes occurring at different locations in the porous medium. In particular, the process occurring upstream near the

injection point corresponds to fresh injected fluid contacting evolving, trapped reservoir fluid and the process occurring downstream near the advancing front crudely corresponds to evolved injected fluid contacting fresh reservoir fluid. These different processes are shown in Figs. 5(c) and 5(d). If miscibility develops via the first of these processes, it is referred to as a condensing gas drive in EOR, while if miscibility develops via the second it is referred to as a vaporizing gas drive. Our previous work used an artificial microchannel design holding a single pocket of trapped fluid to interrogate both processes separately [22]. In contrast, here both processes are observed simultaneously.

Upstream, the behavior is quite different for the four different injection compositions shown. This can be linked back to the evolution trajectories in the ternary diagram, as described above and shown in Fig. 5(c). For pure water and 90% water, the two phases remain immiscible with sharp intensity profiles and static flow structures. Conversely, for 82% and 81% water concentration, there was sufficient time for a significant transfer of water from the injected fluid into the trapped reservoir fluid, and miscibility has started to develop. Visually this is seen as smoother intensity profiles across the interface in this region as shown in Fig. 5(b).

In contrast, downstream, the behaviors are quite similar for the four different compositions of the injected fluid, especially at the advancing tip. In all cases, a sharp intensity profile is maintained across the interface with comparable invasion structures. This can also be linked to the predicted compositional evolution [shown in the ternary diagram in Fig. 5(d)]. For pure water, the injected fluid absorbs ethanol during continual contact with fresh reservoir fluid to reach a composition of approximately 90% water, 10% ethanol. The dilution line between the injected fluid with 90% water concentration coincides with a tie line and this composition does not evolve. For 82% and 81% water concentration, the injected fluid rejects ethanol during continual contact with fresh reservoir fluid and again reaches a composition of approximately 90% water, 10% ethanol. Thus after some time, all four cases have the same evolved composition of the injected fluid at the tip, which is immiscible with fresh reservoir fluid, and thus the invasion behavior is similar. Note that the time stamps for comparison in Fig. 5 are different because more of the upstream region is invaded for lower water

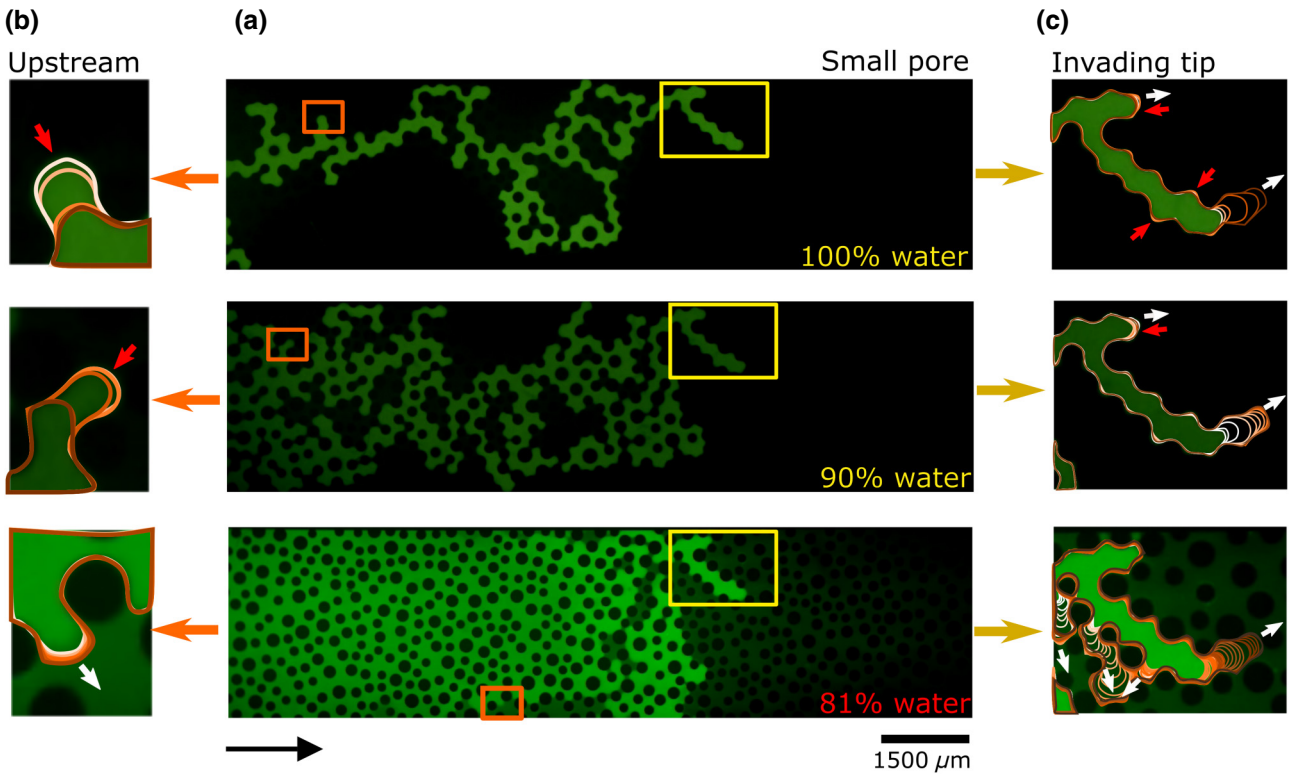

FIG. 6. (a) Experimental images for a wetting reservoir phase of initial composition 35% ethanol, 65% hexanol (uncolored or black) and injected fluid compositions: 100% water 90% water and 81% water at 12 μl/h injection rate (containing green fluorescein). (b)–(c) Interface locations at 0.2-s time intervals for the three different concentrations. White arrows indicate invasion and red arrows indicate retraction. The time over which the invading tip location is shown is 1 s for 100% water, 2 s for 90% water, and 10.4 s for 81% water. Different colors are attributed to the line of the leading edge for clarity.

concentration and so the tip reaches the same location at different times.

B. Dynamics at the pore scale

Figure 6 shows the movement of the interface at the pore scale for a variety of compositions. The white arrows indicate locations where the interface advances, while the red arrows indicate locations where the interface retracts. The time interval between each colored leading edge is 1 s for 100% water, 2 s for 90% water, and 10.4 s for 81% water. The pure water case (top row) in Fig. 6(c) shows clear evidence of Haines jumps at the advancing tip, with the injected fluid advancing abruptly in one pore while retreating in neighbors. These episodic advances can result in an avalanche of pore filling at the tip while inhibiting pore filling upstream, or even causing retreat upstream [46,48–51]. These Haines jumps become less prominent as the composition shifts towards miscibility: the immiscible, 90% water case has less prominent jumps and the interfaces advance a little less abruptly compared to the 100% case, while the MCM, 81% water case has multiple-pore invasion and a smooth progression of the interfaces at the tip. As shown in Fig. 6(b), an interface at upstream retreated abruptly in the 100% and 90% cases due to the sudden jump at the invading tip, whereas the retreating phenomenon almost disappeared at upstream in the 81% water case. We postulate that despite the similarity of the compositions at the tip [see Fig. 5(d)], the long-range cooperation evident in Haines jumps is impacted by the divergent evolution occurring upstream [see Fig. 5(c)].

C. Impact of porosity

Experiments to characterize the effect of porosity are carried out at low flow rates for three different porosity values: 62% (small pores), 67% (medium pores), and 72% (large pores). The porosity is changed by altering the size of the pillars, but not their locations, to interrogate the impact of porosity in isolation of heterogeneity of the porous medium. Therefore, the change of porosity here does not include the impact of different porous structures.

We begin by comparing the displacement paths in the three different porosity cases during the injection of pure water. The preferential paths of those cases are quantified by fractal dimension using box-counting methods as shown in Fig. 7(b). At the same concentration (same color code), there is a very similar fractal dimension value with different porosity, indicating the preferential path is pore size independent over the range tested. As shown in the first row of Fig. 7(a), all three sizes have a nearly identical displacement path. This is because, at these flow rates, invasion proceeds into the pore with the lowest capillary entry pressure and these are identical in our experimental schema. The only difference arises from one missing pillar for the two smaller pillar sizes where a narrow gap could not be manufactured near the wall. The experimentally observed pathway is in excellent agreement with the pathway predicted in our simulation and suggests that these experiments are truly in the invasion-percolation regime.

Considering now the interplay between multiple-contact miscibility and pore sizes, shown in Fig. 7(a), we note that there are relatively small differences in the preferential path for different pore sizes. The invading front for 82% and 81% advances similarly. Upstream, larger pore throats appear to promote mass transfer between the injected fluid and the trapped reservoir fluid and thus develop miscibility slightly more readily, but it only has a limited impact on the saturation level. Thus, we conclude that the effect of porosity is relatively small over the range we consider.

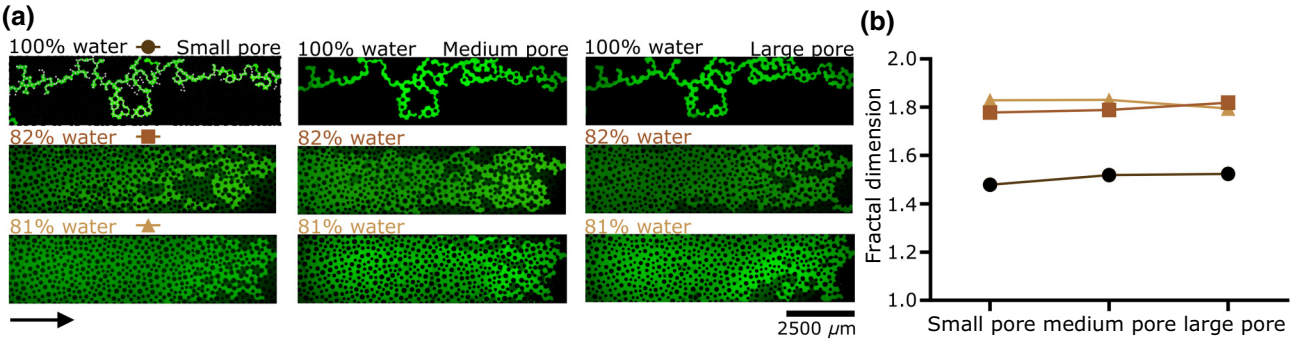

FIG. 7. (a) Experimental images comparing displacements with different pore sizes for a wetting reservoir fluid (uncolored or black) displaced by a nonwetting injected fluid (containing green fluorescein) of different compositions. The reservoir fluid has an initial composition of 65% hexanol, 35% ethanol. The injected fluid compositions are 100% water (top row); 82% water, 18% ethanol (middle row); and 81% water, 19% ethanol (bottom row). The images are at the instant of breakthrough. The simulated displacement path for the small-pore chip for invasion percolation is indicated by the light blue dots in the first panel of the top row. The brightness of the original image has been adjusted in this case to contrast with the simulated path. (b) Fractal dimension measurements of breakthrough invasion paths of 100% water (dark brown circle), 82% water (medium brown square), and 81% water cases (light brown triangle).

D. Flow rates

In contrast, increasing the flow rate and hence the capillary number has a significant effect on the displacement behavior. Figure 8 shows the evolution after breakthrough at three different flow rates for an injected fluid with 83% water. At this composition, the injected and reservoir phases are predicted to remain immiscible. For the lowest flow rate, trapped pockets of reservoir fluid remain stationary, although some mass transfer is evident in the changing volumes. For the intermediate flow rate, such pockets in the interior of the channel are swept downstream, although those at the edge remain trapped. At the largest flow rates, almost all of the trapped reservoir fluid is swept downstream as viscous forces are sufficient to overcome the relatively weak capillary forces between the evolved phases. This behavior is distinct from that observed with increasing flow rate for immiscible fluids in which there is no mass transfer between the phases. In the latter case, the flow transitions from capillary fingering to near-stable displacement as the capillary number increases from 10^{-6} to 10^{-4}, consistent with the results of Zhang *et al.* [4]. However, the remaining trapped pockets of reservoir fluid remain stationary at all three flow rates and do not evolve. A montage of images for a range of compositions is provided within the Supplemental Material [52].

In conjunction with this behavioral change, Fig. 9(a) shows the evolution of the phase saturation for different compositions and injection flow rates as a function of time. Here a rescaled time is used, $\tau = (t - t_{\mathrm{br}})/t_{\mathrm{th}}$, with t_{br} the time at which the injected fluid first reaches the end of the region of interest and t_{th} the theoretical time at which breakthrough would occur in complete, stable displacement. The overarching trend is for the sweep efficiency to increase as more ethanol is added to the injected phase. For systems that remain immiscible, a second pronounced trend is that the saturation increases with flow rate. For MCM systems, the trend with flow rate is more complex.

For pure water, 90% water and 83% water at the lowest flow rates (light gray symbols), the saturation first drops after breakthrough. This reflects interface retraction

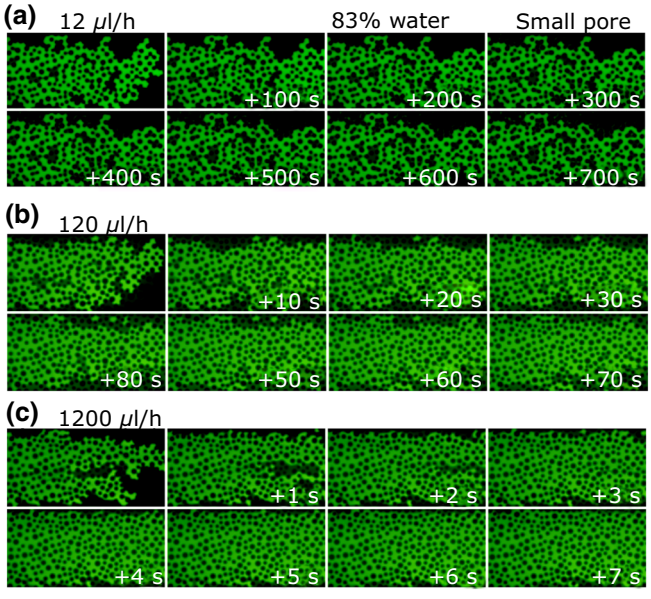

FIG. 8. (a)–(c) Experimental snapshots for a nonwetting injected phase (containing green fluorescein) of initial composition 83% water, 17% ethanol, and three different injection rates.

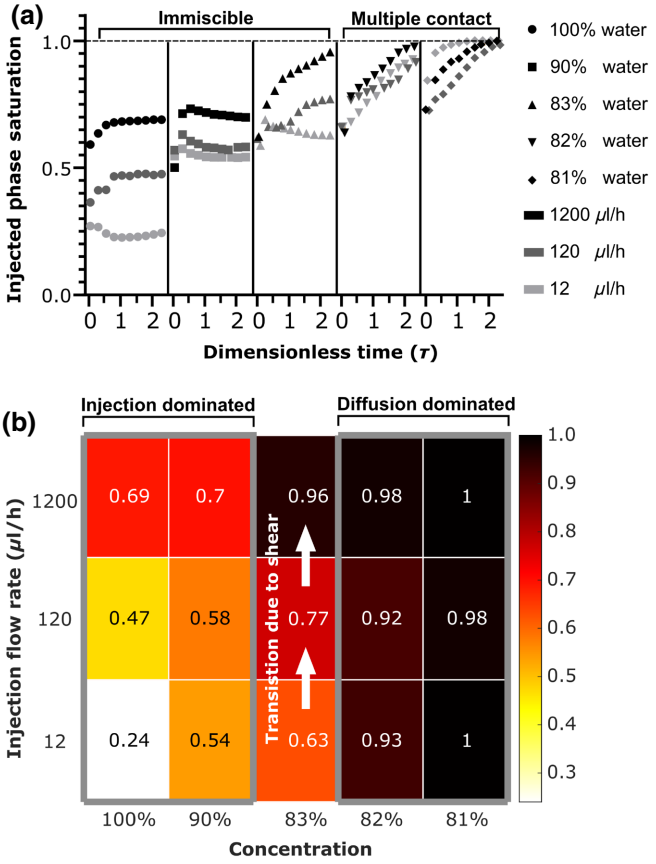

FIG. 9. (a) Phase saturation of the injected fluid as a function of rescaled time for different flow rates (color) and different injection compositions (symbols). The plot is divided into two regions, namely, immiscible and MCM. In the immiscible region, three concentrations of injected fluid are shown: 100% water, 90% water, and 83% water. In the MCM region, two concentrations of injected fluid are shown: 82% water (which is the limit of the MCM region) and 81%. For each concentration, three different flow rates, 12 μL/hr (gray), 120 μL/hr (dark gray), and 1200 μl/h (black), are plotted. The initial composition of the reservoir fluid is 35% ethanol, 65% hexanol, and the data is for the small-pore chip. (b) Segmentation diagram of injection flow rate against concentration. The final saturation at $\tau \approx 2.4$ is represented in a color-scale mapping. The diagram is divided into three regions: injection dominated, transition due to shear, and diffusion dominated.

upstream during pore invasion downstream. After this, the saturation level plateaus with the residual reservoir fluid remaining trapped in the pockets that formed during the initial invasion stage. Despite the structural similarity in the saturation curves, there is a 30% difference in the plateau values between pure water and 90% water. We postulate that this large change results from both the reduction in interfacial tension and the reservoir phase changing from strongly to weakly wetting [24].

In the case of 100% water, an increased flow rate results in a substantial difference in the final saturation, commensurate with viscous effects allowing smaller pores to be invaded and the front to advance in a more stable manner. For 90% water, this difference remains but is significantly less pronounced, such that at the highest flow rates there is little difference in the saturation level between the two concentrations. At the lower flow rate, there is more time (during initial invasion) for phase evolution to take place, in turn affecting the wettability of fluid and viscosity ratio between two phases.

Higher shear forces at higher flow rates significantly increase the phase saturation, because higher pressure gradients allow more widespread pore invasion. However, the curves for the 100% and 90% water cases at 1200 μl/h still plateau, because strong interfacial tension retains some reservoir fluid in the pore space. However, a distinct change occurs for the intermediate- and high-flow-rate cases with 83% water. This is because the shear force becomes dominant and the interfacial tension cannot retain the trapped reservoir fluid in pockets. The ability to remove reservoir fluid within the porous medium is largely affected by the shear force applied even if the system is not developing miscibility. Therefore in Fig. 9(b), the 100% and 90% water cases are categorized as injection dominated and 83% water is a transition case due to shear forces.

A dramatic transition for the 12 μl/h cases (diffusion dominant) is observed between 83% and 82% water. At 83%, a plateau saturation value is reached, while at 82%, there is a continual, steady drift in the saturation level as miscibility develops. In the diffusion-dominated cases (flow rates of 12 μl/h), the saturation level heavily depends on the change in composition between the two phases, in turn affecting whether fluid can be retained in the pocket. As the ethanol concentration increases, the rate of developing miscibility increases. The 81%-water curves with different flow rates converge at $\tau \approx 2.4$ whereas a small discrepancy between the saturation level exists for 81% water cases at $\tau \approx 2.4$. Furthermore, the position of saturation level between 12 μl/h and 1200 μl/h is swapped from 82% to 81% water. Such a transition shows that the diffusion applies more impact on saturation level than shear forces during multiple-contact miscibility development whereas the significance of the impact is the opposite for immiscible displacement.

In the flow-rate experiments, the key features observed is the transition region due to shear at 83%. The injection flow rate has significant impact on saturation level for 100% and 90% water due to viscous effects. The first transition occurred at the 83% water case. At this concentration, the ability to retain the reservoir fluid in the pocket reduces, which results in a continuous saturation level increase under higher injection flow rate. When the system is developing miscibility, the impact of shear flow is minimized and the saturation level is heavily affected by composition evolution between two phases, in turn affecting the ability to retain the fluid in the pocket. For the second transition, it is observed that the impact of diffusion overtakes the impact of shear force at 81% water.

IV. CONCLUSION

Our work is a first step at extending the classical parameter-space diagram of Lenormand *et al.* [6] for drainage to ternary systems in which multiple-contact miscibility can develop. Figure 10 is a superposition of our observations and the classical regime diagram of Lenormand *et al.* [6], showing conceptually how the displacement regime observed along the path of the invading fluid varies as the composition changes. The current challenge is to plot this quantitatively by measuring the phase compositions and interfacial tensions within the microfluidic device during miscibility development. Our work shows the distinct transition behavior from the capillary fingering regime towards stable displacement due to miscibility development.

A microfluidic porous medium with a random distribution of pillars is created to mimic physical heterogeneity. Our experiments explore the injection of nonwetting fluids of varying compositions into a porous medium filled with a wetting reservoir fluid of fixed composition. The injected-fluid composition covered the immiscible, MCM, and FCM regimes. The randomness in the medium is repeated in such a way that pillar locations are the same, but the size of each pillar is scaled. This method allows us to interrogate the impact of porosity in isolation of heterogeneity of the porous medium. We explore 2 orders of magnitude in capillary numbers.

The displacement has five distinct behaviors for different compositions: (i) capillary fingering for immiscible systems in which strong interfacial tension is maintained, (ii) displacement more similar to stable immiscible displacement for systems in which the interfacial tension is reduced but not eliminated, (iii) near-MCM systems in which displacement near the advancing front remains immiscible while behind the front interfaces remain but the trapped fluid is mobilized, (iv) MCM systems in which displacement near the advancing front remains immiscible while behind the front miscibility develops and interfaces disappear, and (v) FCM systems in which no interfaces

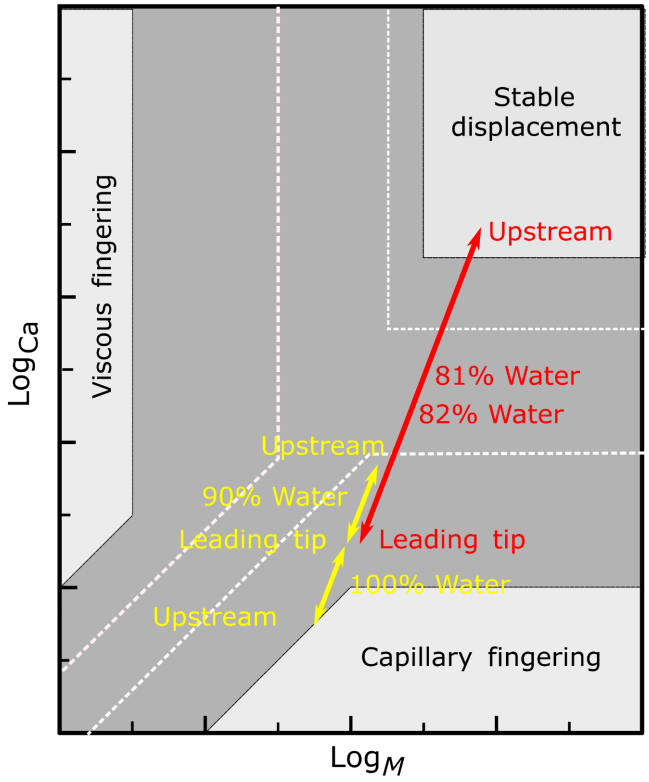

FIG. 10. Conceptual image for multiple contact miscible systems characterized by two dimensionless numbers: the capillary number (Ca) and the viscosity ratio (M). Immiscible cases are indicated by yellow color and MCM cases are indicated by red color. The displacement regimes are based on existing work [4,6].

exist. We observe only behavior class (iii) for the highest-flow rate experiments, in which shear is sufficient to overcome the weak interfacial tension between the two phases. We postulate that this regime is absent entirely for the lowest flow rates and applies for a progressively broader range of compositions for increasing flow rates. With accurate interfacial tension measurements on the binodal curve, it would be interesting to map out the evolution of the capillary number and compare the behaviors observed with immiscible flows at the same values. We leave this to future work. The effect of porosity is minimal over the range we explore, with identical displacement pathways for pure water and qualitatively identical behavior for other compositions.

By extending the classical parameter-space diagram to a partially miscible ternary system, it opens a better understanding of miscibility development in drainage for CO_2-EOR applications. At the same time, this work also shows the application of microfluidics for oil and gas industry. We hope this work can inspire more researchers to use the microfluidic platform to connect the fundamental study and practical application in the energy field.

ACKNOWLEDGMENTS

This work was performed in part at the Melbourne Centre for Nanofabrication (MCN) in the Victorian Node of the Australian National Fabrication Facility (ANFF).

[1] A. Anbari, H.-T. Chien, S. S. Datta, W. Deng, D. A. Weitz, and J. Fan, Microfluidic model porous media: Fabrication and applications, Small **14**, 1703575 (2018).
[2] X. Zheng, N. Mahabadi, T. S. Yun, and J. Jang, Effect of capillary and viscous force on CO_2 saturation and invasion pattern in the microfluidic chip, J. Geophys. Res.: Solid Earth **122**, 1634 (2017).
[3] F. Guo and S. A. Aryana, An experimental investigation of flow regimes in imbibition and drainage using a microfluidic platform, Energies **12**, 1390 (2019).
[4] C. Zhang, M. Oostrom, T. W. Wietsma, J. W. Grate, and M. G. Warner, Influence of viscous and capillary forces on immiscible fluid displacement: Pore-scale experimental study in a water-wet micromodel demonstrating viscous and capillary fingering, Energy Fuels **25**, 3493 (2011).
[5] R. Lenormand, Liquids in porous media, J. Phys.: Condens. Matter **2**, SA79 (1990).
[6] R. Lenormand, E. Touboul, and C. Zarcone, Numerical models and experiments on immiscible displacements in porous media, J. Fluid Mech. **189**, 165 (1988).
[7] Y. Wang, C. Zhang, N. Wei, M. Oostrom, T. W. Wietsma, X. Li, and A. Bonneville, Experimental study of crossover from capillary to viscous fingering for supercritical CO_2-water displacement in a homogeneous pore network, Environ. Sci. Technol. **47**, 212 (2013).
[8] K. J. DeHoff, M. Oostrom, C. Zhang, and J. W. Grate, Evaluation of two-phase relative permeability and capillary pressure relations for unstable displacements in a pore network, Vadose Zone J. **11**, vzj2012 (2012).
[9] R. Holtzman and E. Segre, Wettability Stabilizes Fluid Invasion Into Porous Media via Nonlocal, Cooperative Pore Filling, Phys. Rev. Lett. **115**, 164501 (2015).
[10] B. Zhao, C. W. MacMinn, and R. Juanes, Wettability control on multiphase flow in patterned microfluidics, Proc. Natl. Acad. Sci. USA **113**, 10251 (2016).
[11] H. A. Koch, Jr. and R. L. Slobod, Miscible slug process, Trans. AIME **210**, 40 (1957).
[12] R. Rommerskirchen, P. Nijssen, H. Bilgili, and T. Sottmann, in *Abu Dhabi International Petroleum Exhibition & Conference* (Society of Petroleum Engineers, Abu Dhabi, UAE, 2016).
[13] R. Rommerskirchen, H. Bilgili, J. Fischer, and T. Sottmann, in *SPE Improved Oil Recovery Conference* (Society of Petroleum Engineers, Tulsa, Oklahoma, USA, 2018).
[14] C. Hutchinson, Jr. and P. H. Braun, Phase relations of miscible displacement in oil recovery, AIChE J. **7**, 64 (1961).
[15] A. Zick, in *SPE Annual Technical Conference and Exhibition* (Society of Petroleum Engineers, New Orleans, Louisiana, USA, 1986).
[16] F. I. Stalkup, in *SPE Annual Technical Conference and Exhibition* (Society of Petroleum Engineers, Dallas, Texas, USA, 1987).

[17] F. M. Orr, *Theory of Gas Injection Processes* (Tie-Line Publications Copenhagen, Copenhagen, Denmark, 2007), Vol. 5.

[18] A. Bahadori, *Fundamentals of Enhanced Oil and Gas Recovery from Conventional and Unconventional Reservoirs* (Gulf Professional Publishing, Oxford, UK, 2018).

[19] K. Ahmadi Rahmataba, Ph.D. thesis, The University of Texas at Austin, 2011.

[20] I. Bahralolom, R. Bretz, and F. Orr, Jr., Experimental investigation of the interaction of phase behavior with microscopic heterogeneity in a CO_2 flood, SPE Reservoir Eng. **3**, 662 (1988).

[21] Y. M. Al-Wahaibi, First-contact-miscible and multicontact-miscible gas injection within a channeling heterogeneity system, Energy Fuels **24**, 1813 (2010).

[22] H. Zou, A. C. Slim, and A. Neild, Rapid characterization of multiple-contact miscibility: Toward a slim-tube on a chip, Anal. Chem. **91**, 13681 (2019).

[23] A. Sharbatian, A. Abedini, Z. Qi, and D. Sinton, Full characterization of CO_2-oil properties on-chip: Solubility, diffusivity, extraction pressure, miscibility, and contact angle, Anal. Chem. **90**, 2461 (2018).

[24] H. Zou, H. Kang, A. Slim, and A. Neild, Pore-scale multiple-contact miscibility in a microfluidic chip, Lab Chip **20**, 3582 (2020).

[25] J. N. Lee, C. Park, and G. M. Whitesides, Solvent compatibility of poly (dimethylsiloxane)-based microfluidic devices, Anal. Chem. **75**, 6544 (2003).

[26] F. G. Helfferich, Theory of multicomponent, multiphase displacement in porous media, Soc. Pet. Eng. J. **21**, 51 (1981).

[27] G. J. Hirasaki, Application of the theory of multicomponent, multiphase displacement to three-component, two-phase surfactant flooding, Soc. Pet. Eng. J. **21**, 191 (1981).

[28] Y. M. Al-Wahaibi, A. H. Muggeridge, and C. A. Grattoni, Experimental and numerical studies of gas/oil multicontact miscible displacements in homogeneous and crossbedded porous media, SPE J. **12**, 62 (2007).

[29] Y. M. Al-Wahaibi, A. H. Muggeridge, and C. A. Grattoni, Gas–oil non-equilibrium in multicontact miscible displacements within homogeneous porous media, J. Pet. Sci. Eng. **68**, 71 (2009).

[30] T. C. LaForce, Y. Cinar, R. T. Johns, and F. M. Orr, Jr., Experimental confirmation for analytical composition routes in three-phase partially miscible flow, SPE J. **15**, 160 (2010).

[31] D. A. DiCarlo, K. Jessen, and F. M. Orr, Compositional gravity drainage 2: Experimental measurements using an analog system, Transp. Porous Media **69**, 159 (2007).

[32] I. C. Morrow, R. Norman, and J. J. Taber, Entrapment and mobilization of residual oil in bead packs, SPE Reservoir Eng. **3**, 927 (1988).

[33] D. Schechter, D. Zhou, and F. Orr, Jr., Low IFT drainage and imbibition, J. Pet. Sci. Eng. **11**, 283 (1994).

[34] G. Wang, G. Pickup, K. Sorbie, E. Mackay, and A. Skauge, Multi-physics approach to modelling near-miscible CO_2-WAG process, J. Pet. Sci. Eng. **198**, 108165 (2021).

[35] H.-m. Lin, G.-B. Hong, C.-E. Yeh, and M.-J. Lee, Liquid-liquid equilibria for ternary mixtures of water+ ethanol with 1-hexanol, butyl propionate, or ethyl caproate, J. Chem. Eng. Data **48**, 587 (2003).

[36] D. Villers and J. Platten, Temperature dependence of the interfacial tension between water and long-chain alcohols, J. Phys. Chem. **92**, 4023 (1988).

[37] I. S. Khattab, F. Bandarkar, M. A. A. Fakhree, and A. Jouyban, Density, viscosity, and surface tension of water+ ethanol mixtures from 293 to 323 K, Korean J. Chem. Eng. **29**, 812 (2012).

[38] J. J. Cano-Goómez, G. A. Iglesias-Silva, E. O. Castrejoón-Gonzaólez, M. Ramos-Estrada, and K. R. Hall, Density and viscosity of binary liquid mixtures of ethanol + 1-hexanol and ethanol + 1-heptanol from (293.15 to 328.15) K at 0.1 MPa, J. Chem. Eng. Data **60**, 1945 (2015).

[39] A. Karperien, Fraclac for imagej, http://rsb.info.nih.gov/ij/plugins/fraclac/FLHelp/Introduction.htm (1999–2013).

[40] V. Berejnov, A. Bazylak, D. Sinton, and N. Djilali, Fractal flow patterns in hydrophobic microfluidic pore networks: Experimental modeling of two-phase flow in porous electrodes, J. Electrochem. Soc. **157**, B760 (2010).

[41] D. Wilkinson and J. F. Willemsen, Invasion percolation: A new form of percolation theory, J. Phys. A: Math. Gen. **16**, 3365 (1983).

[42] R. Lenormand and S. Bories, Description of a bond percolation mechanism used for the simulation of drainage with trapping in porous-media, C. R. Seances Acad. Sci., Ser. B **291**, 279 (1980).

[43] L. Furuberg, J. Feder, A. Aharony, and T. Jøssang, Dynamics of Invasion Percolation, Phys. Rev. Lett. **61**, 2117 (1988).

[44] R. Lenormand and C. Zarcone, Capillary fingering: Percolation and fractal dimension, Transp. Porous Media **4**, 599 (1989).

[45] R. Chandler, J. Koplik, K. Lerman, and J. F. Willemsen, Capillary displacement and percolation in porous media, J. Fluid Mech. **119**, 249 (1982).

[46] R. T. Armstrong and S. Berg, Interfacial velocities and capillary pressure gradients during haines jumps, Phys. Rev. E **88**, 043010 (2013).

[47] S. Berg, H. Ott, S. A. Klapp, A. Schwing, R. Neiteler, N. Brussee, A. Makurat, L. Leu, F. Enzmann, J.-O. Schwarz, M. Kersten, S. Irvine, and M. Stampanoni, Real-time 3D imaging of haines jumps in porous media flow, PNAS USA **110**, 3755 (2013).

[48] A. Alhosani, A. Scanziani, Q. Lin, S. Foroughi, A. M. Alhammadi, M. J. Blunt, and B. Bijeljic, Dynamics of water injection in an oil-wet reservoir rock at subsurface conditions: Invasion patterns and pore-filling events, Phys. Rev. E **102**, 023110 (2020).

[49] K. J. Måløy, L. Furuberg, J. Feder, and T. Jøssang, Dynamics of Slow Drainage in Porous Media, Phys. Rev. Lett. **68**, 2161 (1992).

[50] Z. Sun and J. C. Santamarina, Haines jumps: Pore scale mechanisms, Phys. Rev. E **100**, 023115 (2019).

[51] F. Moebius and D. Or, Interfacial jumps and pressure bursts during fluid displacement in interacting irregular capillaries, J. Colloid Interface Sci. **377**, 406 (2012).

[52] See Supplemental Material at http://link.aps.org/supplemental/10.1103/PhysRevApplied.15.054040 for detailed images for Figs. 4 and 5, and experimental images comparing displacements with different injection rate.